Greening of the Earth and its drivers

Zaichun Zhu[1,2], Shilong Piao[1,2*], Ranga B. Myneni[3], Mengtian Huang[2], Zhenzhong Zeng[2], Josep G. Canadell[4], Philippe Ciais[5], Stephen Sitch[6], Pierre Friedlingstein[7], Almut Arneth[8], Chunxiang Cao[9], Lei Cheng[10], Etsushi Kato[11], Charles Koven[12], Yue Li[2], Xu Lian[2], Yongwen Liu[2], Ronggao Liu[13], Jiafu Mao[14], Yaozhong Pan[15], Shushi Peng[2], Josep Peñuelas[16,17], Benjamin Poulter[18,19], Thomas A. M. Pugh[8], Benjamin D. Stocker[20], Nicolas Viovy[5], Xuhui Wang[2], Yingping Wang[21], Zhiqiang Xiao[22], Hui Yang[2], Sönke Zaehle[23], Ning Zeng[24]

[1] Institute of Tibetan Plateau Research, Center for Excellence in Tibetan Earth Science, Chinese Academy of Sciences, Beijing 100085, China.

[2] Sino-French Institute for Earth System Science, College of Urban and Environmental Sciences, Peking University, Beijing 100871, China

[3] Department of Earth and Environment, Boston University, Boston, Massachusetts 02215, USA

[4] Global Carbon Project, CSIRO Oceans and Atmosphere, GPO Box 3023, Canberra, ACT 2601, Australia

[5] Laboratoire des Sciences du Climat et de l'Environnement (LSCE), CEA CNRS UVSQ, 91191 Gif Sur Yvette, France.

[6] College of Engineering, Computing and Mathematics, University of Exeter, Exeter EX4 4QF, UK.

[7] College of Engineering, Mathematics and Physical Sciences, University of Exeter, Exeter EX4 4QF, UK

[8] Institute of Meteorology and Climate Research, Atmospheric Environmental Research, Karlsruhe Institute of Technology, 82467 Garmisch-Partenkirchen, Germany.

[9] State Key Laboratory of Remote Sensing Science, Institute of Remote Sensing and Digital Earth, Chinese Academy of Sciences, Beijing 100101, China

[10] CSIRO Land and Water, Black Mountain, Canberra, ACT 2601, Australia

[11] Institute of Applied Energy (IAE), Minato-ku, Tokyo 105-0003, Japan

[12] Earth Sciences Division, Lawrence Berkeley National Lab, 1 Cyclotron Road, Berkeley, CA 94720, USA

[13] Institute of Geographic Sciences and Natural Resources Research, Chinese Academy of Sciences, Beijing, 100101, China

[14] Climate Change Science Institute and Environmental Sciences Division, Oak Ridge National Laboratory, Oak Ridge, TN, USA

[15] College of Resources Science & Technology, State Key Laboratory of Earth Processes and Resource Ecology, Beijing Normal University, Beijing 100875, China

[16] CSIC, Global Ecology Unit CREAF-CEAB-UAB, Cerdanyola del Vallès, 08193 Catalonia, Spain

[17] CREAF, Cerdanyola del Vallès, 08193 Catalonia, Spain

[18] Montana State University, Institute on Ecosystems and the Department of Ecology, Bozeman, Montana 59717, USA.

[19] Laboratoire des Sciences du Climat et de l'Environnement (LSCE), CEA CNRS UVSQ, 91191 Gif Sur Yvette, France.

[20] Department of Life Sciences, Imperial College London, Silwood Park, Ascot, SL5 7PY, UK

[21] CSIRO Ocean and Atmosphere, PMB #1, Aspendale, Victoria 3195, Australia

[22] State Key Laboratory of Remote Sensing Science, School of Geography, Beijing Normal University, Beijing 100875, China

[23] Max-Planck-Institut für Biogeochemie, P.O. Box 600164, Hans-Knöll-Str. 10, 07745 Jena, Germany

[24] Department of Atmospheric and Oceanic Science, University of Maryland, College Park, MD 20742, US

*Correspondence to: Shilong Piao, slpiao@pku.edu.cn

Supplementary Information

S1. GIMMS LAI3g

The Global Inventory Modeling and Mapping Studies (GIMMS) LAI was generated by an Artificial Neural Network (ANN) model and the third generation AVHRR GIMMS NDVI data set[1, 2]. The ANN model was first trained with overlapping AVHRR GIMMS NDVI3g data set and best-quality MODIS LAI, and then generate the full temporal coverage GIMMS LAI3g data set using AVHRR GIMMS NDVI3g. The quality and research applicability of GIMMS LAI3g data set were evaluated through direct comparisons with field data and indirectly through inter-comparisons with similar satellite-data products and statistical analysis with climatic variables and ENSO/AO indices[1]. The GIMMS LAI3g data set, that provides LAI observations at 15-day temporal resolution and 1/12 degree spatial resolution for the global vegetation from July 1981 to December 2014, has been widely used in various research purposes[3, 4, 5, 6]. We first composited the 15-day GIMMS LAI3g data to monthly temporal resolution by averaging the two composites in the same month, and then resampled the GIMMS LAI3g data to 0.5° spatial resolution using the bicubic method.

S2. GLASS LAI

The Global Land Surface Satellite (GLASS) LAI data set was derived from AVHRR, MODIS and CYCLOPES reflectance and LAI products using general regression neural networks[7]. The GLASS LAI provides global LAI products at 8-day temporal resolution and 1km spatial resolution from 1981 to 2012 in the Integer zed Sinusoidal projection (http://www.bnu-datacenter.com/). The validation against CYCLOPES and MODIS LAI products, as well as field measurements confirms the applicability of GLASS LAI product in long-term study of global vegetation dynamics. We first composited the 8-day GIMMS LAI3g data to monthly temporal resolution by averaging the composites in the same month. Before the averaging process, we weighted each composite by the number of days that the composites fall in the given month. Then, we resampled the GLASS LAI3g data to 0.5° spatial resolution using the

bicubic method.

S3. GLOBMAP LAI

The Global Mapping LAI product was generated by quantitative fusion of MODIS and historical AVHRR data[8]. The pixel-level relationship between AVHRR and MODIS LAI was first established for the overlapping period 2000-2006 and then used to construct AVHRR LAI back to 1981. The constructed AVHRR LAI and MODIS LAI were combined, which provide a global LAI data set at 15-day temporal resolution and 8km spatial resolution for the period 1981 to 2009 (http://www.globalmapping.org/globalLAI/). We preprocessed the GLOBMAP LAI using the same method as we used to preprocess the GIMMS LAI3g data set.

S4. MEaSUREs FT-ESDR

The Freeze/Thaw Earth System Data Record (FT-ESDR) is a NASA Making Earth System Data Records for Use in Research Environments (MEaSUREs) funded effort to provide a consistent daily global data record of land surface freeze/thaw (FT) state dynamics for all vegetated regions that extends 34 years (1979 to 2012)[9, 10]. The FT-ESDR data set was derived from overlapping daily radiometric brightness temperature measurements at 37 GHz frequency from the Scanning Multichannel Microwave Radiometer (SMMR), Special Sensor Microwave Imager (SSM/I) sensor series and the Advanced Microwave Scanning Radiometer for EOS (AMSR-E).

S5. Growing season integrated leaf area index

The growing season integrated leaf area index (hereafter refer to LAI) has been found to be a good proxy of vegetation primary production[11]. The growing season duration is evaluated in each vegetated pixel as follows. The Savitzky-Golay filter is first used to smooth the LAI3g data because it maintains the distinctive vegetation time series trajectories and minimizes various atmospheric effects[12, 13]. The smoothed 15-day LAI3g time series is interpolated to daily LAI3g time series using linear interpolation. From the daily LAI3g time series, the LAI-based growing season is determined as: (a) the “start day” is the day when the LAI value is greater than 0.1 and

has increased by 15% of the amplitude of the growing season; (b) the "end day" is the day when the LAI value is greater than 0.1 and has decreased by 15% of the amplitude of the growing season; (c) the length of growing season is the duration between start day and end day of the growing season. This threshold-based growing season requires refinement in the northern latitudes because the vegetation may remain green during the dormant season due to sub-optimal temperatures and low sunlight levels. The period when the vegetation is actually photosynthetically active is determined by the freeze/thaw state of the ground[14], which can be assessed from satellite measurements of passive microwave brightness temperatures[10]. Fig. S1 shows the global spatial distributions of average start date and duration of growing season for the period 1982 to 2009. A comparison of LAI3g integrated over the growing season thus defined with up-scaled flux tower measurements of gross primary production (GPP) showed good correspondence (Fig. S2). This correspondence gives confidence in treating LAI as a proxy for GPP.

S6. Uncertainties in satellite observed LAI

GIMMS LAI3g, GLASS LAI and GLOBMAP LAI are 3 widely used long-term LAI products that provide global LAI records start from the middle of 1981. These 3 LAI data were derived from the legacy AVHRR and MODIS data using different methodologies[15]. All 3 LAI products have been extensively validated against field measurements and other satellite products, which warrant their suitability of long-term vegetation research. However, we should also pay attention to uncertainties in the 3 LAI products. Although all the 3 LAI products consistently show the dominant greening trends over global vegetated area, the spatial distribution and magnitudes of LAI trends are somewhat different (Fig. 1). There are several reasons that may account for the discrepancies and uncertainties in the 3 LAI products. First, the 3 LAI products were generated using different strategies and different AVHRR products[1, 7, 8] . Second, the AVHRR sensors lack of on-board calibration and have orbital loss problem, which caused biases that are difficult to be quantified[2, 16]. Third, although GLASS LAI and GLOBMAP LAI proposed their own methods to merge LAI derived from AVHRR

sensors and MODIS, it is still difficult to create a consistent LAI time series because AVHRR and MODIS sensors have different spectral characteristics[16, 17]. These problems are supposed to be solved by generating accurate and consistent LAI time series data in the future. Nevertheless, at present, the 3 LAI products have irreplaceable value to study long-term vegetation research. The 3 LAI data sets were used for detection and attribution of trends in LAI during 1982 to 2009. Specifically, GIMMS LAI3g, the longest remotely sensed LAI data we have, were used to illustrate a continued greening (up to 2014) of global vegetation.

S7. Process-based ecosystem models

Global monthly LAI for the period 1982 to 2009 simulated by 10 ecosystem models were used in this analysis (Table S1). Seven of the models were coordinated by the project "Trends and drivers of the regional scale sources and sinks of carbon dioxide" (TRENDY, http://dgvm.ceh.ac.uk/node/9)[18]. Simulations of other 3 models (CLM4, CABLE and VEGAS) were performed under the similar protocol but for the period 1982 to 2009. We analyzed data for the period 1982-2009 for which we had access to both satellite observation and outputs from model simulations. All the model outputs were resampled to a common spatial resolution (0.5°) using the nearest neighbor method.

The global ecosystem models were forced with historical changes in atmospheric CO_2 concentration, climate, nitrogen deposition (in 5 models, Table S1) and land cover change (in 7 models, Table S1). Generally, most ecosystem models that used in our study represented photosynthesis based on Farquhar model. The Farquhar model is a well-established biochemical model that estimates the enzyme kinetics of Rubisco, the main enzyme limiting photosynthesis, based on availability of light, temperature and CO_2 concentration in leaf. Although the ecosystem models used similar photosynthesis model, they differ a lot in subcomponents. For example, stomatal conductance model varies between the global ecosystem models. The global ecosystem models represent phenology through the growing degree day (GDD) concept that controlled by

temperature and soil moisture. However, the parameterizations of their phenology module can differ greatly and affect growing season integrated leaf are index. The Plant Function Type (PFT) is a key concept that allowing for the reduction of thousands of species to a small set of functional groups defined by their phenology type, physiognomy, photosynthetic pathway, and climate zone. PFTs that used by global ecosystem models are sometimes different[19]. For example, ORCHIDEE defined 12 PFTs and used a PFT map that generated by combining simplified Olson biomes with IGBP GLCC data[20], while LPJ defined 10 PFTs[21]. Fig. S4 shows the Taylor diagrams that compare the ten available ecosystem models to the satellite observation from 1982 to 2009 at the global scales and continental scales. Fig. S5 shows trends in global averaged LAI derived from individual model simulations driven by rising CO_2, climate change, nitrogen deposition and land cover change using Mann-Kendal test. Fig. S6 shows the spatial pattern of trends in LAI simulated by individual models under the same scenario S2 (varying CO_2 and climate). Both of these figures indicate that there are obvious differences in modeling LAI among the ecosystem models used in our study. All the 7 global ecosystem models in TRENDY group represent deforestation, afforestation and to some extent regrowth (Table S2) [18]. These processes are the most important component of land cover change. The global ecosystem models used a consistent land cover change data[22]. This land cover change data set not only provides annual fractional data on primary vegetation and secondary vegetation at 0.5 degree spatial resolution, but also underlines transitions between land cover states. Typically, the models only used the information about changes in agricultural areas although the land cover change data also provides the information about changes in the non-agricultural areas. The models generally implement this processes differently. For example, an increased cropland fraction in a grid cell can either be at the expense of grassland, or forest (i.e. deforestation)[18].

All models performed simulations S1 and S2 using global atmospheric CO_2 concentration[23] and historical climate fields from CRU-NCEP data set[24]. In simulation S1, models were forced with changing atmospheric CO_2 concentration, while climate

was held constant (recycling climate mean and variability from 1901 to 1920). Both atmospheric CO_2 concentration and climate were varied in simulation S2. Two models (CLM4 and CABLE) performed an additional simulation (S3) that atmospheric CO_2 concentration, climate, and nitrogen deposition were all varied. The average difference of S3 and S2 of CLM4 and CABLE was used to assess the relative contribution of nitrogen deposition. The 7 TRENDY models performed an additional scenario that CO_2 concentration, climate and land-cover were all varied (S4). The difference of S4 and S2 were used to evaluate the response of vegetation growth to land use and land cover change. Table S3 lists the responses of LAI that simulated by each individual model to CO_2, climate change, nitrogen deposition and land cover change.

S8. Changes in observed maximum LAI (LAI_{max})

We performed similar trend analyses for the observed LAI_{max}. The results show that LAI_{max} from 3 long-term satellite LAI data sets also consistently show positive trends over a large portion of the global vegetated area during the study period (Figure S7). The patterns of trends in LAI_{max} are similar to that of the trends in growing season LAI. The global greening trend in LAI_{max} estimated from the three data sets is 0.012 ± 0.005 $m^2m^{-2}yr^{-1}$. The regions with the largest LAI_{max} greening trends, consistent across the 3 data sets, are in Northern Amazon, Europe, Central Africa and Southeast Asia. The GLASS LAI_{max} data shows the most extensive statistically significant increases (Mann-Kendal test, $p<0.05$) over 58.6% of vegetated lands, followed by GLOBMAP LAI_{max} (43.5%) and GIMMS $LAI3g_{max}$ (29.3%). All 3 LAI data sets also consistently show a decreasing LAI_{max} trend over less than 3% of global vegetated land.

S9. Trends in biosphere parameters that may affect LAI trends

Five of the TRENDY2 models (CLM4.5, LPX-Bern, LPJ, LPJ-GUESS and VISIT) provided outputs of gross primary productivity (GPP), net primary productivity (NPP), autotrophic respiration (RA) and carbon emissions due to fires (Cfire). With these outputs, we were able to explore which of these variables exhibit trends related to those of LAI (Fig. S8). According to model simulations, we found that GPP, NPP and RA all

show statistically significant ($p<0.05$) increasing trends, while Cfire show statistically significant decreasing trend. The model simulations suggest that increasing GPP, although partly neutralized by increasing RA, and decreasing Cfire are responsible for the increasing LAI during 1982 to 2009.

According to model simulations, increases in GPP, NPP and RA and decreases in Cfire due to direct and indirect effects of increasing atmospheric CO_2 concentration are all statistically significant ($p<0.05$). The models also show that increasing atmospheric CO_2 concentration contributes the most to increases in GPP, NPP and RA, while LCC effects were the major factor that caused the decrease in Cfire. Climate change statistically significantly stimulated GPP of global vegetation during our study period. However, RA change caused by climate change also statistically significantly increased. These trends almost compensate each other, making the climate-induced change of NPP statistically not significant. The magnitude of Cfire trends is much smaller than trends in GPP, NPP or RA during 1982 to 2009, which suggests that decreasing fires loss was not a major cause of LAI increase. Satellite-based burned area data show that the ratio of global annual burned area to global vegetated area is about 3% and trend in global burned area is about -1% per year [25]. Such a small fraction combined with its small trends also suggest the limited role of Satellite-observed burned area data also confirmed the limited role of Cfire in affecting global vegetation.

S10. Differences between the spatial pattern of trends in modeled LAI and observed LAI

We noticed that the inconsistencies between observations and models are mainly in the Southwestern United States, Southern South American countries, and Mongolia (Fig. 3a and b). In these regions, MMEM suggests that LAI has strongly decreased for the period 1982 to 2009, whereas observation suggests little decreasing or even slightly increasing trends. To investigate the possible reason that caused the differences, we first checked the model fractional simulations. We found that these negative trends were mainly caused by climate change (Fig. S11b). We further investigated which climatic

factor is most responsible for the negative trends using an additional simulation experiment with ORCHIDEE (Section S13). ORCHIDEE simulation driven by climate change only generally captured the strong negative trends as shown in Fig. S9a. The fractional simulations of ORCHIDEE suggest that trends in precipitation are the dominant driving factor that account for the strong decreasing trends in model-simulated LAI (Fig. S9b). We also investigated the global pattern of annual total precipitation using observed precipitation data (CRU). The results show that the (red) regions where simulated LAI decreased in MMEM model simulations match well with the regions where annual total precipitation significantly decreased (Fig. S9c).

Such pronounced negative trends were not captured by any of the three satellite products. Our analysis indicated that models may be over-sensitive to trends in precipitation as soil water holding capacities maybe under-estimated in models, and deep rooting, ecosystem composition changes (e.g. shrubification) are not modeled, which is consistent with previous studies[26].

S11. Optimal Fingerprints Analysis

We used an optimal fingerprint method to detect the relative contribution of each external driving factor to the observed change in vegetation activity[27, 28]. The optimal fingerprint expresses the observation (Y) as a linear combination of scaled (β_i) responses to external driving factors (x_i), which were estimated using ecosystem models, and internal variability (ε):

$$\mathrm{Y} = \sum_{i=1}^{n} \beta_i x_i + \varepsilon$$

In this study, the LAI simulated by ecosystem models was used to estimate the vegetation change response to external forcing, i.e. CO_2 fertilization, climate change, nitrogen deposition and land cover change. Specifically, we used 3 satellite data to calculate the mean LAI. And 10, 10, 2 and 7 simulations (Table S1) were used to calculate the ensemble mean LAI signals driven by CO_2 fertilization, climate change, nitrogen deposition and land cover change, respectively. Satellite observed LAI and

multi-model ensemble mean LAI driven by each external forcing were first aggregated onto global or continental scale and then averaged over 2-year window. The internal variability of changes in vegetation growth was estimated using CMIP5 model control run simulations (Table S4) and preprocessed similar to the signals of external forcings. All the satellite observed LAI and model simulated LAI are centered by subtracting their mean value. We regressed the satellite observed change in LAI onto the multi-model ensemble mean LAI driven by CO_2 fertilization, climate change, nitrogen deposition and land cover change and estimated their scaling factors using the total least square method[28]. We also performed similar analysis for the simulated LAI under scenarios S1, S2, S3 and S4. The 95% confidence interval of the estimated scaling factor lies above zero indicates that the signal of the corresponding driving factor is detected. And the corresponding signal is suitable for attribution if the 95% confidence interval contains 1.

S12. Analysis of CO_2 fertilization effects based on simple concept model

The water-use efficiency of photosynthesis is defined as the ratio of the rates of assimilation (A) and transpiration (E) per unit of leaf area[29]:

$$\mathrm{W} = \frac{A}{E} = \frac{C_a}{1.6v}\left(1 - \frac{C_i}{C_a}\right) \quad (1)$$

where v, C_i and C_a are the leaf-to-air water vapor-pressure deficit and the intercellular and atmospheric CO_2 concentrations, respectively. The relative effect of a change in C_a on W is given by:

$$\frac{dW}{W} = \frac{dA}{A} - \frac{dE}{E} = \frac{dC_a}{C_a} - \frac{dv}{v} + \frac{d\left(1-\frac{C_i}{C_a}\right)}{\left(1-\frac{C_i}{C_a}\right)} \quad (2)$$

The quantity $(1 - C_i/C_a)$ has been modeled and observed as being proportional to the square root of the vapor-pressure deficit $(\sqrt{v})$[30, 31,32]. Thus:

$$\frac{dW}{W} = \frac{dA}{A} - \frac{dE}{E} = \frac{dC_a}{C_a} - \frac{1}{2}\frac{dv}{v} \quad (3)$$

E can be written as:

$$E = 1.6 g_s v \quad (4)$$

The relative effects of changes in g_s and v can be expressed as:

$$\frac{dE}{E} = \frac{dg_s}{g_s} + \frac{dv}{v} \quad (5)$$

Equation 3 can thus be written as:

$$\frac{dW}{W} = \frac{dA}{A} - \frac{dg_s}{g_s} - \frac{dv}{v} = \frac{dC_a}{C_a} - \frac{1}{2}\frac{dv}{v} \quad (6)$$

and

$$\frac{dA}{A} = \frac{dC_a}{C_a} + \frac{1}{2}\frac{dv}{v} + \frac{dg_s}{g_s} \quad (7)$$

Atmospheric CO_2 concentrations (Ca) increased from 341 to 387 ppm (~46 ppm) during 1982-2009[33], i.e. dC_a/C_a was 13.5%. We also calculated monthly vapor-pressure deficits for the study period using the CRU time-series data [34]. The vapor-pressure deficit was calculated from the difference between saturated vapor pressure, which was calculated using monthly mean temperature, and the monthly mean vapor-pressure data provided by the CRU time series. The results suggested that the relative change of annual mean vapor-pressure deficit over vegetated areas globally (dv/v) was about 2.3% for 1982-2009. The experimentally measured response of stomatal conductance to elevated C_a suggested that an increase in C_a of 46 ppm would cause a relative change in stomatal conductance (dg_s/g_s) of -5.0 to -3.0%[35, 36]. We estimated from equation (7) a relative change of A of about 9.7-11.7% (or 21.1-25.4% per 100 ppm). We also estimated from equation (6) a relative change of W of about 12.3%. The results indicated that the direct (dC_a/C_a) and indirect (dg_s/g_s) effects of an increase in C_a were the major factors that affected the change in A during 1982-2009 (8.5-10.5%, or 18.5-22.8% per 100 ppm).

We also estimated the relative change of global GPP using the 7 TRENDY2 models. The TRENDY2 models suggested that the relative change of GPP during the study period was 5.2-8.3% (11.3-18.0% per 100 ppm), which is comparable to the relative change of GPP estimated by the above simple conceptual leaf-scale model. The

simulated modeled results were also comparable to the relative changes inferred from the Free-Air CO_2 Enrichment (FACE) experiments. The increase in C_a during 1982-2009 from the FACE experiment[37] led to an increase in NPP of 6.1-9.4% (or 9.5-20.4% per 100 ppm) and an increase in LAI of 0.3-11.1% (or 0.6-24.1% per 100 ppm), and the TRENDY2 models estimated relative increases in global NPP and LAI of 5.2-9.0% (or 11.3-19.6% per 100 ppm) and 4.7-9.5% (or 10.2-20.7% per 100 ppm), respectively. Our study, however, referenced few FACE experimental sites, which were mainly in forested regions and thus did not represent the heterogeneity of the CO_2 fertilization effects across all representative vegetation types (or model PFTs).

The generally comparable relative changes of global vegetation growth estimated from the simple conceptual models, the ecosystem models, and the FACE experiments lend credibility to our estimates of the response of global vegetation to elevated C_a during 1982-2009. Various complex mechanisms control the responses of vegetation growth to C_a, which are (to some extent) represented in our models. Analyzing all these mechanisms from model simulations under predefined scenarios, however, is difficult. The simple conceptual model identified some major mechanisms that control the responses of vegetation to C_a. The theoretical method, however, assumes the absence of other factors such as nutrient limitations or disturbances. Further research on the interactive mechanisms between the CO_2 fertilization effects and other factors is needed.

S13. Partitioning climate change effects

To further understand the response of vegetation trend to climate change, we designed an additional set of scenarios for ORCHIDEE: (ORC_S1) varying atmospheric CO_2 concentration and varying climate; (ORC_S2) varying CO_2, precipitation and radiation; (ORC_S3) varying CO_2, temperature and radiation; (ORC_S4) varying CO_2, temperature and precipitation. We accessed the effects of temperature, precipitation and radiation by subtracting ORC_S2, ORC_S3 and ORC_S4 from ORC_S1, respectively.

Given that there were large differences in model-simulated responses to changing

environmental factors, we implemented a two-step analysis to decompose the dominant role of climate change in driving LAI trends. First, we used MMEM to determine the dominant factor that accounts for increasing/decreasing trend in LAI for each vegetated pixel (Fig. 3c). From this analysis, we can determine the pixels where trends (increasing or decreasing) in LAI were dominated by 'climate change'. Then, we further decomposed 'climate change' into climate variables (temperature, precipitation and radiation) in pixels that were dominated by 'climate change' using additional specific simulations from ORCHIDEE (Fig. S13). This analysis helped determine the dominant climate variables in the pixels where climate change is the dominant factor as suggested by the MMEM simulations.

References

1. Zhu ZC, Bi J, Pan YZ, Ganguly S, Anav A, Xu L*, et al.* Global data sets of vegetation leaf area index (LAI)3g and fraction of photosynthetically active radiation (FPAR)3g derived from global inventory modeling and mapping studies (GIMMS) normalized difference vegetation index (NDVI3g) for the period 1981 to 2011. *Remote Sens-Basel* **5**, 927-948 (2013).
2. Pinzon J, Tucker C. A non-stationary 1981–2012 AVHRR NDVI3g time series. *Remote Sens-Basel* **6**, 6929-6960 (2014).
3. Anav A, Friedlingstein P, Kidston M, Bopp L, Ciais P, Cox P*, et al.* Evaluating the land and ocean components of the global carbon cycle in the CMIP5 earth system models. *J. Climate* **26**, 6801-6843 (2013).
4. Cook BI, Pau S. A global assessment of long-term greening and browning trends in pasture lands using the GIMMS LAI3g dataset. *Remote Sens-Basel* **5**, 2492-2512 (2013).
5. Poulter B, Frank D, Ciais P, Myneni RB, Andela N, Bi J*, et al.* Contribution of semi-arid ecosystems to interannual variability of the global carbon cycle. *Nature* **509**, 600-603 (2014).
6. Piao S, Nan H, Huntingford C, Ciais P, Friedlingstein P, Sitch S*, et al.* Evidence for a weakening relationship between interannual temperature variability and northern vegetation activity. *Nat. Commun.* **5**, 5018-5018 (2014).
7. Xiao ZQ, Liang SL, Wang JD, Chen P, Yin XJ, Zhang LQ*, et al.* Use of general regression neural networks for generating the GLASS leaf area index product from time-series modis surface reflectance. *IEEE T. Geosci. Remote* **52**, 209-223 (2014).
8. Liu Y, Liu RG, Chen JM. Retrospective retrieval of long-term consistent global leaf area index (1981-2011) from combined AVHRR and MODIS data. *J. Geophys. Res. Biogeosci.* **117**, 440-440 (2012).
9. Kim Y, Kimball JS, Zhang K, McDonald KC. Satellite detection of increasing northern hemisphere non-frozen seasons from 1979 to 2008: Implications for regional vegetation growth. *Remote Sens. Environ.* **121**, 472-487 (2012).

10. Kim Y, Kimball JS, McDonald KC, Glassy J. Developing a global data record of daily landscape freeze/thaw status using satellite passive microwave remote sensing. *IEEE T. Geosci. Remote* **49**, 949-960 (2011).
11. Prince SD. Satellite remote-sensing of primary production - comparison of results for sahelian grasslands 1981-1988. *Int. J. Remote Sens.* **12**, 1301-1311 (1991).
12. Chen J, Jonsson P, Tamura M, Gu ZH, Matsushita B, Eklundh L. A simple method for reconstructing a high-quality ndvi time-series data set based on the Savitzky-Golay filter. *Remote Sens. Environ.* **91**, 332-344 (2004).
13. Jonsson P, Eklundh L. Timesat - a program for analyzing time-series of satellite sensor data. *Comput. Geosci-UK* **30**, 833-845 (2004).
14. McDonald KC, Kimball JS, Njoku E, Zimmermann R, Zhao MS. Variability in springtime thaw in the terrestrial high latitudes: Monitoring a major control on the biospheric assimilation of atmospheric CO_2 with spaceborne microwave remote sensing. *Earth Interact.* **8**, 1-23 (2004).
15. Fang H, Jiang C, Li W, Wei S, Baret F, Chen JM*, et al.* Characterization and intercomparison of global moderate resolution leaf area index (LAI) products: analysis of climatologies and theoretical uncertainties. *J. Geophys. Res. Biogeosci.* **118**, 529-548 (2013).
16. Tucker CJ, Pinzon JE, Brown ME, Slayback DA, Pak EW, Mahoney R*, et al.* An extended AVHRR 8−km NDVI dataset compatible with modis and spot vegetation ndvi data. *Int. J. Remote Sens.* **26**, 4485-4498 (2005).
17. Guay KC, Beck PSA, Berner LT, Goetz SJ, Baccini A, Buermann W. Vegetation productivity patterns at high northern latitudes: A multi-sensor satellite data assessment. *Glob. Change Biol.* **20**, 3147-3158 (2014).
18. Le Quéré C, Peters GP, Andres RJ, Andrew RM, Boden T, Ciais P*, et al.* Global carbon budget 2013. *Earth Syst. Sci. Data Discuss.* **6**, 689-760 (2013).
19. Poulter B, Ciais P, Hodson E, Lischke H, Maignan F, Plummer S*, et al.* Plant functional type mapping for earth system models. *Geosci. Model Dev.* **4**, 993-1010 (2011).
20. Krinner G, Viovy N, de Noblet-Ducoudre N, Ogee J, Polcher J, Friedlingstein P*,*

et al. A dynamic global vegetation model for studies of the coupled atmosphere-biosphere system. *Glob. Biogeochem. Cycles* **19**, GB1015 (2005).

21. Sitch S, Smith B, Prentice IC, Arneth A, Bondeau A, Cramer W*, et al.* Evaluation of ecosystem dynamics, plant geography and terrestrial carbon cycling in the LPJ dynamic global vegetation model. *Glob. Change Biol.* **9**, 161-185 (2003).
22. Hurtt GC, Chini LP, Frolking S, Betts RA, Feddema J, Fischer G*, et al.* Harmonization of land-use scenarios for the period 1500–2100: 600 years of global gridded annual land-use transitions, wood harvest, and resulting secondary lands. *Climatic Change*, **109**, 117-161 (2011).
23. Keeling, C. D. & Whorf, T. P. Atmospheric CO_2 records from sites in the SIO air sampling network. In *Trends: A Compendium of Data on Global Change* (Carbon Dioxide Information Analysis Center, Oak Ridge National Laboratory, US DOE, 2005)
24. New M, Hulme M, Jones P. Representing twentieth-century space-time climate variability. Part ii: Development of 1901-96 monthly grids of terrestrial surface climate. *J. Climate*, **13**, 2217-2238 (2000).
25. Giglio L, Randerson JT, van der Werf GR. Analysis of daily, monthly, and annual burned area using the fourth-generation global fire emissions database (GFED4). *J. Geophys. Res. Biogeosci.* **118**, 317-328 (2013).
26. Piao SL, Sitch S, Ciais P, Friedlingstein P, Peylin P, Wang XH*, et al.* Evaluation of terrestrial carbon cycle models for their response to climate variability and to CO_2 trends. *Glob. Change Biol.* **19,** 2117-2132 (2013).
27. Allen MR, Stott PA. Estimating signal amplitudes in optimal fingerprinting, part i: Theory. *Clim. Dynam.* **21**, 477-491 (2003).
28. Allen MR, Tett SFB. Checking for model consistency in optimal fingerprinting. *Clim. Dynam.* **15,** 419-434 (1999).
29. Wong SC, Cowan IR, Farquhar GD. Stomatal conductance correlates with photosynthetic capacity. *Nature* **282**, 424-426 (1979).
30. Farquhar GD, Lloyd J, Taylor JA, Flanagan LB, Syvertsen JP, Hubick KT*, et al.* Vegetation effects on the isotope composition of oxygen in atmospheric CO_2.

Nature **363**, 439-443 (1993).

31. Medlyn BE, Duursma RA, Eamus D, Ellsworth DS, Prentice IC, Barton CVM*, et al.* Reconciling the optimal and empirical approaches to modelling stomatal conductance. *Glob. Change Biol.* **17**, 2134-2144 (2011).
32. Donohue RJ, Roderick ML, McVicar TR, Farquhar GD. Impact of CO_2 fertilization on maximum foliage cover across the globe's warm, arid environments. *Geophys. Res. Lett.* **40**, 3031-3035 (2013).
33. Tans P. Trends in atmospheric carbon dioxide. 2015, Available from: www.esrl.noaa.gov/gmd/ccgg/trends/
34. Harris I, Jones PD, Osborn TJ, Lister DH. Updated high-resolution grids of monthly climatic observations - the CRU TS3.10 dataset. *Int. J. Climatol.* **34**, 623-642 (2014).
35. Ainsworth EA, Rogers A. The response of photosynthesis and stomatal conductance to rising CO_2: Mechanisms and environmental interactions. *Plant Cell Environ.* **30**, 258-270 (2007).
36. Field CB, Jackson RB, Mooney HA. Stomatal responses to increased CO_2 - implications from the plant to the global-scale. *Plant Cell Environ.* **18**, 1214-1225 (1995).
37. Norby RJ, DeLucia EH, Gielen B, Calfapietra C, Giardina CP, King JS*, et al.* Forest response to elevated CO_2 is conserved across a broad range of productivity. *Proc. Natl Acad. Sci. USA* **102**, 18052-18056 (2005).
38. Oleson K, Lawrence DM, Bonan GB, Levis S, Swenson S, Thornton PE*, et al.* Technical description of version 4.5 of the community land model (CLM); 2013 July, 01. Report No. NCAR/TN-503+STR.
39. Lindeskog M, Arneth A, Bondeau A, Waha K, Seaquist J, Olin S*, et al.* Implications of accounting for land use in simulations of ecosystem carbon cycling in africa. *Earth Syst. Dynam.* **4**, 385-407 (2013).
40. Stocker BD, Strassmann K, Joos F. Sensitivity of holocene atmospheric CO_2 and the modern carbon budget to early human land use: Analyses with a process-based model. *Biogeosciences* **8,** 69-88 (2011).

41. Zaehle S, Friend AD. Carbon and nitrogen cycle dynamics in the O-CN land surface model: 1. Model description, site-scale evaluation, and sensitivity to parameter estimates. *Global Biogeochem. Cycles 24, GB1006* (2010).
42. Krinner G, Viovy N, de Noblet-Ducoudré N, Ogée J, Polcher J, Friedlingstein P*, et al.* A dynamic global vegetation model for studies of the coupled atmosphere-biosphere system. *Global Biogeochem. Cycles* **19**, GB1015 (2005).
43. Kato E, Kinoshita T, Ito A, Kawamiya M, Yamagata Y. Evaluation of spatially explicit emission scenario of land-use change and biomass burning using a process-based biogeochemical model. *J. Land Use Sci.* **8**, 104-122 (2013).
44. Lawrence DM, Oleson KW, Flanner MG, Thornton PE, Swenson SC, Lawrence PJ*, et al.* Parameterization improvements and functional and structural advances in version 4 of the community land model. *J. Adv. Model. Earth Syst.* 3, M03001 (2011).
45. Wang YP, Law RM, Pak B. A global model of carbon, nitrogen and phosphorus cycles for the terrestrial biosphere. *Biogeosciences* **7,** 2261-2282 (2010).
46. Zeng N, Neelin JD, Chou C. A quasi-equilibrium tropical circulation model - implementation and simulation. *J. Atmos. Sci.* **57**, 1767-1796 (2000).
47. Beer C, Reichstein M, Tomelleri E, Ciais P, Jung M, Carvalhais N*, et al.* Terrestrial gross carbon dioxide uptake: Global distribution and covariation with climate. *Science* **329,** 834-838 (2010).
48. Olson DM, Dinerstein E, Wikramanayake ED, Burgess ND, Powell GVN, Underwood EC*, et al.* Terrestrial ecoregions of the worlds: A new map of life on earth. *Bioscience* **51,** 933-938 (2001).
49. Taylor KE. Summarizing multiple aspects of model performance in a single diagram. *J. Geophys. Res. Atmos.* **106**, 7183-7192 (2001).

Table S1. List of multi-model simulations used in this study.

Models	Source	S1	S2	S3	S4	Carbon-nitrogen interactions	Reference
CLM4.5		yes	yes	no	yes	yes	[38]
LPJ		yes	yes	no	yes	no	[18, 21]
LPJ-GUESS		yes	yes	no	yes	no	[18, 39]
LPX-Bern	TRENDY	yes	yes	no	yes	yes	[40]
OCN		yes	yes	no	yes	yes	[41]
ORCHIDEE		yes	yes	no	yes	no	[42]
VISIT		yes	yes	no	yes	no	[43]
CLM4		yes	yes	yes	no	yes	[44]
CALBE	--	yes	yes	yes	no	yes	[45]
VEGAS		yes	yes	no	no	no	[46]

Table S2. Processes included in the land cover change representation of the TRENDY2 models[18].

	CLM4.5	LPJ	LPJ-GUESS	LPX-Bern	OCN	ORCHIDEE	VISIT
Deforestation, afforestation, forest regrowth after abandonment of agriculture	√	√	√	√	√	√	√
Wood harvest and forest degradation	√						√
Shifting cultivation	√						√
Cropland harvest	√		√	√	√	√	√
Peat fires	√						
Fire simulation and/or suppression	√	√	√	√			√

Table S3. Responses of LAI ($m^2m^{-2}yr^{-1}$) simulated by individual models to elevated atmospheric CO_2 concentration (CO_2), climate change (CLI), nitrogen deposition (NDE) and land cover change (LCC). S1, S2, S3 and S4 represent four scenarios of model simulations that driven by varying CO_2, varying CO_2 and CLI, varying CO_2, CLI and NDE, and varying CO_2, CLI and LCC, respectively. The last row shows the responses of LAI estimated from multi-model ensemble mean (MMEM) to the driving factors.

	S1	**S2**	**S3**	**S4**	**CO_2**	**CLI**	**NDE**	**LUC**
CLM4.5	0.054**	0.050**	--	0.057**	0.054**	-0.004	--	0.007**
LPX-Bern	0.044**	0.047**	--	0.056**	0.044**	0.003	--	0.009
OCN	0.040**	0.057**	--	0.052**	0.040**	0.016**	--	-0.004**
LPJ	0.069**	0.067**	--	0.059**	0.069**	-0.002	--	-0.008
LPJ-GUESS	0.047**	0.036**	--	0.041**	0.047**	-0.010**	--	0.005
ORCHIDEE	0.036**	0.030**	--	0.022**	0.036**	-0.006	--	-0.008**
VISIT	0.089**	0.115**	--	0.133**	0.089**	0.026**	--	0.018**
CLM4	0.034**	0.059**	0.070**	--	0.034**	0.025**	0.011**	--
CABLE	0.053**	0.047**	0.048**	--	0.053**	-0.006**	0.001**	--
VEGAS	0.013**	0.026**	--	--	0.013**	0.013**	--	--
MMEM	0.048**± 0.020	0.053**± 0.025	0.059**± 0.016	0.060**± 0.035	0.048**± 0.020	0.006± 0.014	0.006**± 0.008	0.002± 0.010

Table S4. List of control-run simulations from CMIP5 used in this study.

Models	CTL years (chunks)
ACCESS1-0	500(17)
ACCESS1-3	500(17)
bcc-csm1-1	500(17)
bcc-csm1-1-m	400(14)
CCSM4	1051(37)
CESM1-BGC	500(17)
CESM1-CAM5	319(11)
CESM-FASTCHEM	222(7)
CESM1-WACCM	200(7)
GFDL-CM3	500(17)
GFDL-ESM2G	500(17)
GFDL-ESM2M	500(17)
HadGEM2-CC	240(8)
HadGEM2-ES	577(20)
inmcm4	500(17)
MPI-ESM-LR	1000(35)
MPI-ESM-MR	1000(35)
MPI-ESM-P	1156(41)

Figure S1. 28-year (1982 to 2009) average start day and duration of the growing season. The growing season was first determined by GIMMS LAI3g data set using Savitzky-Golay filter and then refined by excluding the ground-freeze period identified by the Freeze/Thaw Earth System Data Record. In particular, the growing season of evergreen broadleaf forests was set to 12 months and starts in January.

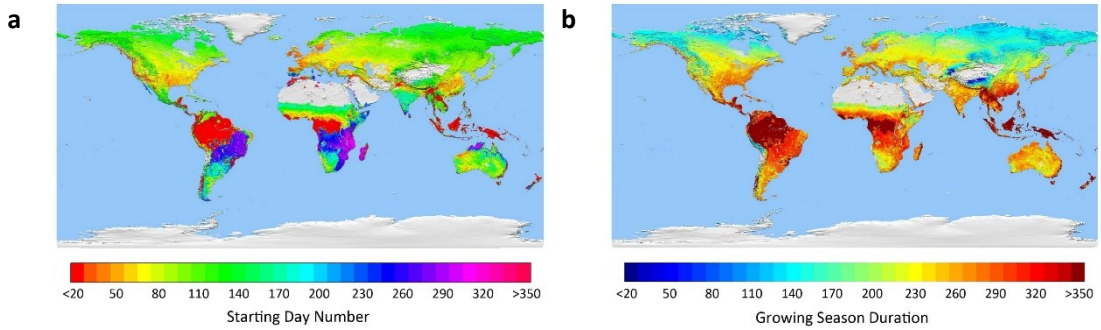

Figure S2. Comparison between 28-year averaged growing season integrated leaf area index (LAI) and GPP product from Beer et al. [47]for 83 terrestrial eco-regions of the world [48]. LAI data for the period 1998 to 2005 were averaged at the pixel level to match the study period of Beer's GPP map. Pixels were weighted by their area in the averaging process at eco-region level to eliminate geometric errors.

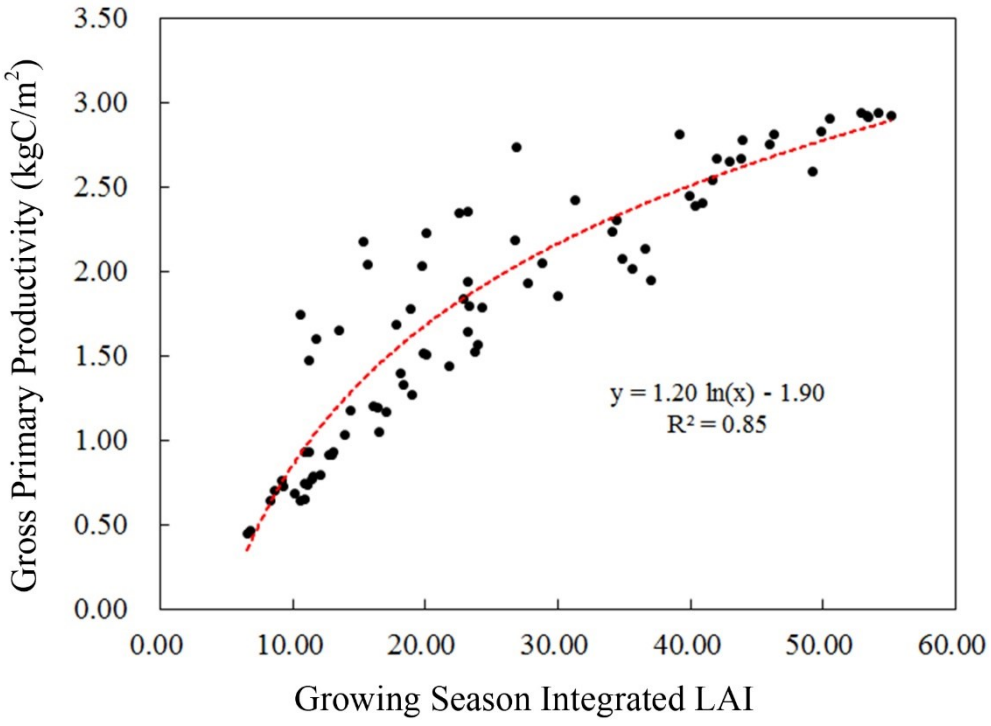

Figure S3. The spatial distribution pattern of trend in growing season integrated LAI derived from GIMMS LAI3g for the period 1982-2014. Regions labeled by black dots indicating those trends are statistically significant (Mann-Kendal test, $p<0.05$). 35% (4%) of the global vegetated area show statistically significant increasing (decreasing) trends. Trend in global LAI derived from GIMMS LAI3g for the period 1982-2014 is 0.032 $m^2m^{-2}yr^{-1}$.

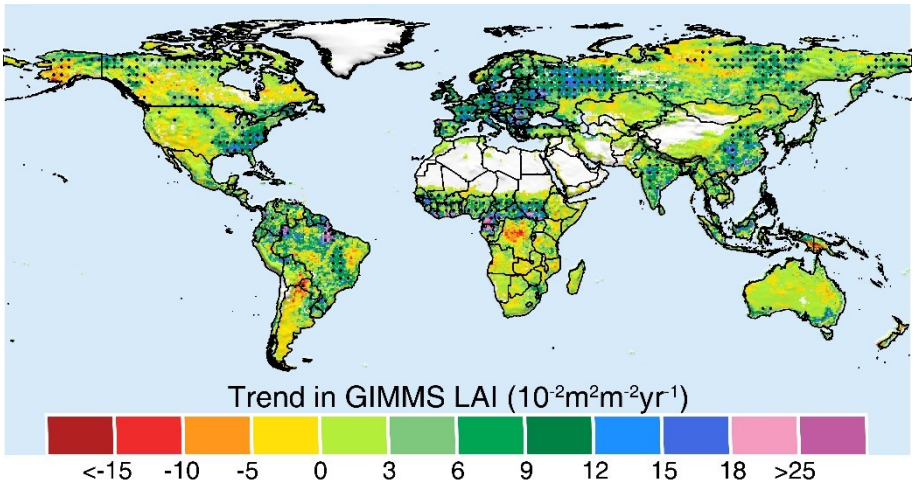

Figure S4. Taylor diagrams compare the ten available Dynamic Global Vegetation Models to the satellite observation from 1982 to 2009 at the global scale (a) and in (b) Africa, (c) Asia, (d) Europe, (e) Oceania, (f) South America, and (g) North America. The standard deviation shows the interannual variability of the observed LAI and the modeled LAI. The dash green lines show centered root mean square difference between model simulations and satellite observation[49].

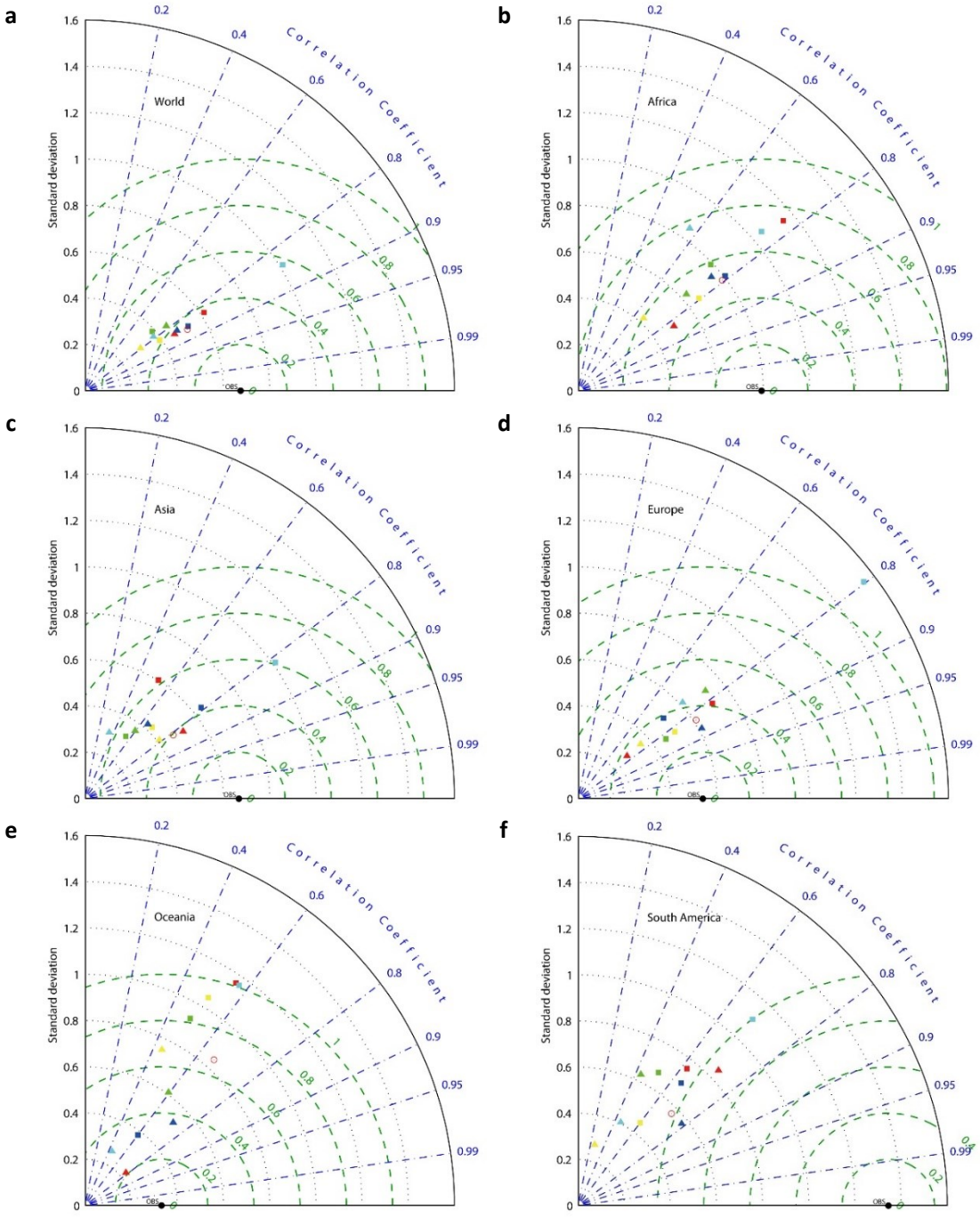

g

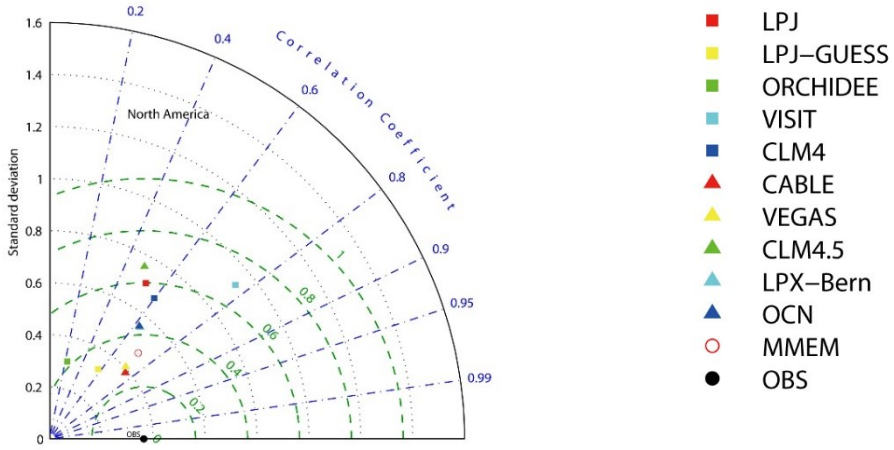
North America
Standard deviation
Correlation Coefficient
0.2
0.4
0.6
0.8
0.9
0.95
0.99
1.6
1.4
1.2
1
0.8
0.6
0.4
0.2
0
OBS
LPJ
LPJ–GUESS
ORCHIDEE
VISIT
CLM4
CABLE
VEGAS
CLM4.5
LPX–Bern
OCN
MMEM
OBS

1

2

3

Figure S5. Trend in global averaged LAI derived from individual model simulations driven by rising CO_2, climate change (CLI), nitrogen deposition (NDE) and land cover change (LCC) using Mann-Kendal test. Error bars show the standard deviation of trends derived from satellite data and model simulations. Two asterisks indicate that the trend is statistically significant ($p<0.05$).

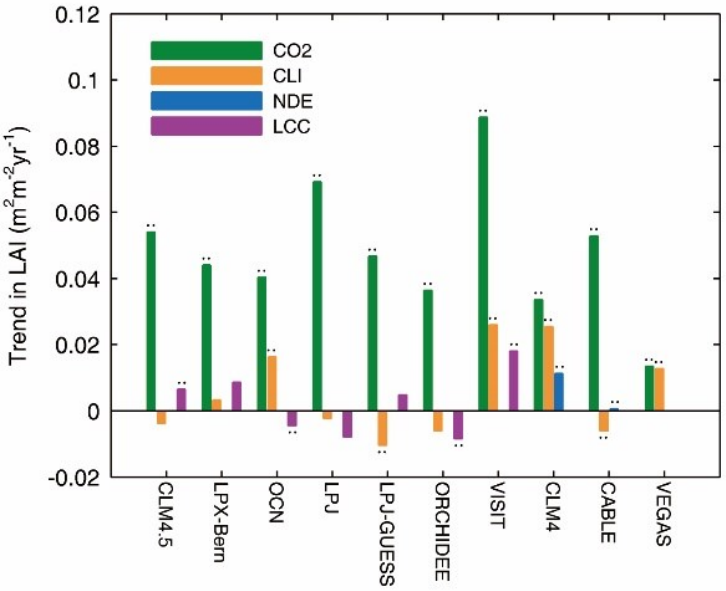

Figure S6. Spatial pattern of trends in LAI simulated by individual models under the same scenario S2 (varying CO_2 and climate).

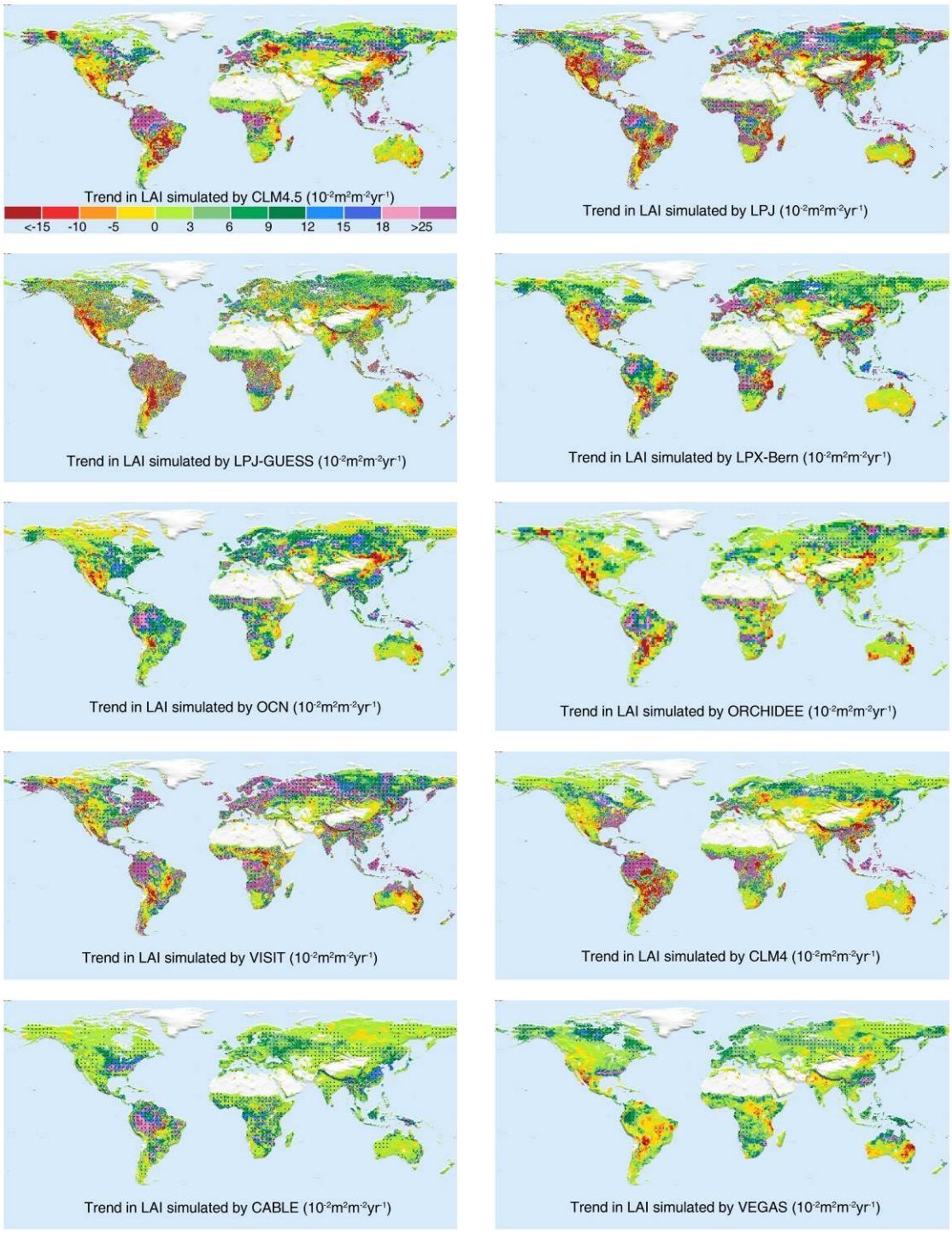

Figure S7. The spatial pattern of trends in maximum LAI of the year (LAI_{max}) derived from three remote sensing data (a) GIMMS LAI3g, (b) GLOBMAP LAI and (c) GLASS LAI. All data sets cover the period 1982 to 2009. Regions labeled by black dots indicate trends that are statistically significant (Mann-Kendal test, $p<0.05$). (d) Probability density function of LAI_{max} trends for GIMMS LAI3g, GLASS LAI, GLOBMAP LAI and the average of the three remote sensing data sets (AVG OBS).

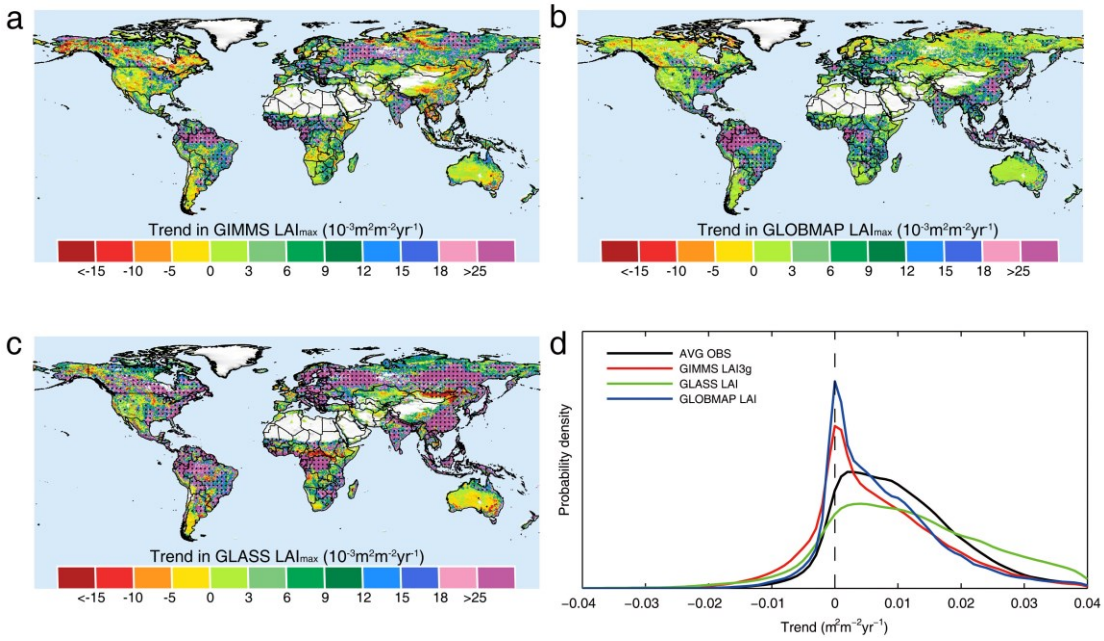

Figure S8. Responses of gross primary productivity (GPP), net primary productivity (NPP), autotrophic respiration (RA) and carbon loss due to fires (Cfire) according to simulations from 5 TRENDY2 models (CLM4.5, LPX-Bern, LPJ, LPJ-GUESS and VISIT). Two asterisks indicate that the trend is statistically significant ($p<0.05$).

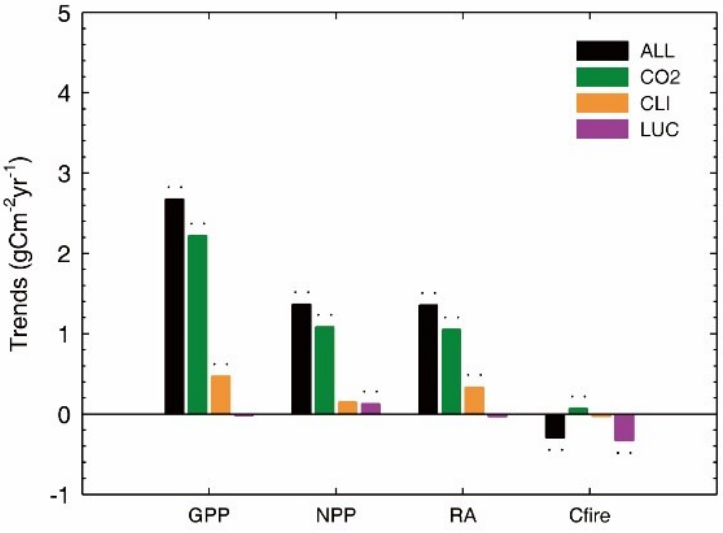

Figure S9. Consistency between satellite observation and model simulations. (a) Trend in LAI due to climate change estimated by ORCHIDEE simulation that account for climate change only; (b) Trend in LAI due to precipitation simulated by ORCHIDEE model; (c) Trend in observed annual total precipitation during 1982 to 2009.

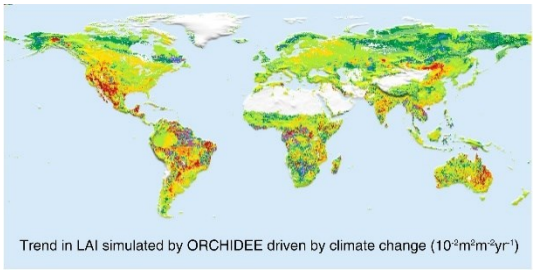

(a)

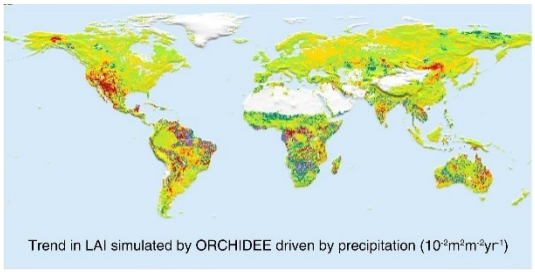

(b)

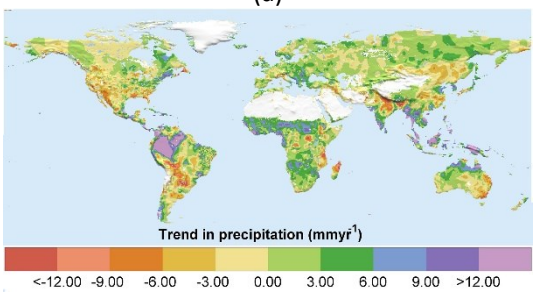

(c)

Figure S10. The first column shows interannual changes in continental anomalies of growing season integrated leaf area index (LAI) estimated by multi-model ensemble mean (MMEM) with all drivers considered and average of 3 remote sensing data. Subfigures (a), (c), (e), (g), (i), (k) shows the results in Africa, Asia, Europe, Oceania, South America and North America, respectively. The shaded area shows the intensity of EI Niño-Southern Oscillation (ENSO) as defined by the multivariate ENSO Index. The black dash lines label the sensors changing time of AVHRR satellite series. Two volcanic eruptions (El Chichón eruption and Pinatubo eruption) were labeled in brown dash lines. The second column shows trend in continental averaged LAI derived from satellite observation (OBS) and modeled trends driven by rising CO_2, climate change (CLI), nitrogen deposition (NDE) and land cover change (LCC) using Mann-Kendal test. Subfigures (b), (d), (f), (h), (j), (l) shows the results in Africa, Asia, Europe, Oceania, South America and North America, respectively. Error bars show the standard deviation of trends derived from satellite data and model simulations. Two asterisks indicate that the trend is statistically significant ($p<0.05$).

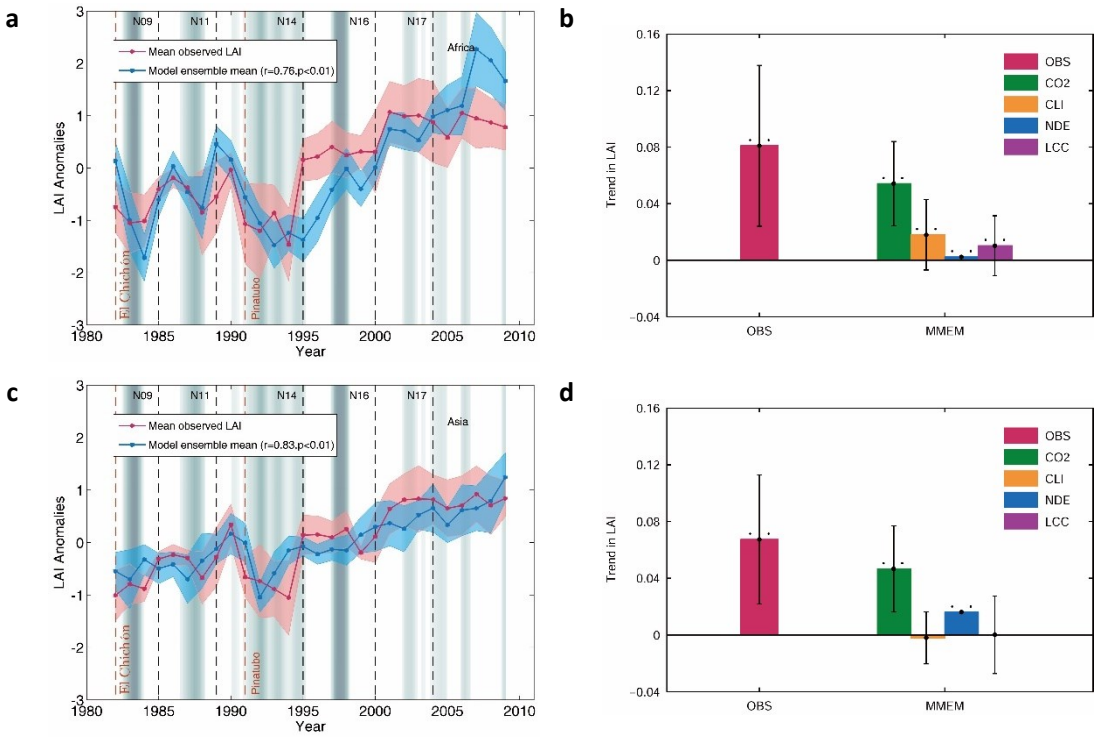

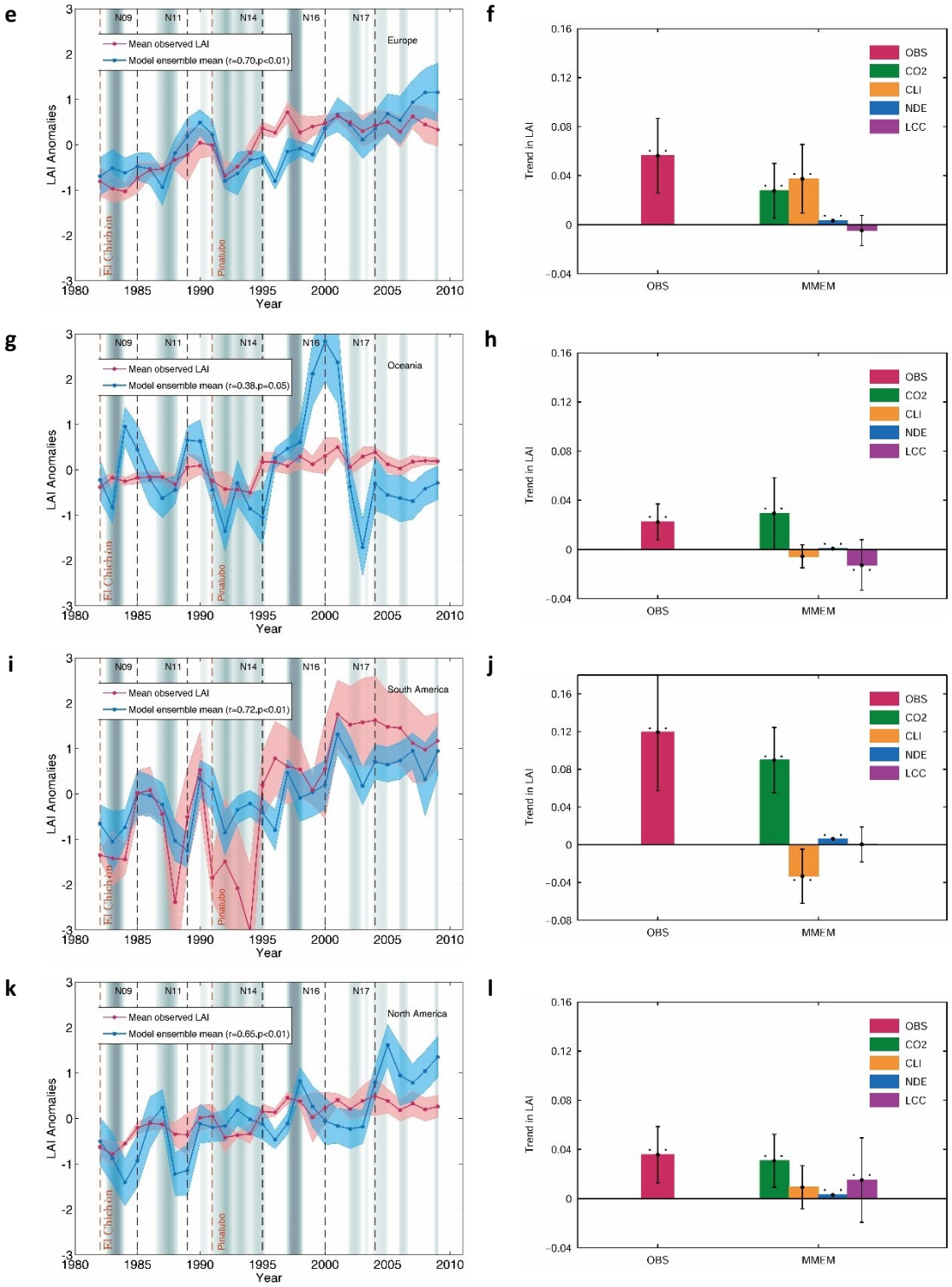
e
f
g
h
i
j
k
l
N09
N11
N14
N16
N17
Mean observed LAI
Model ensemble mean (r=0.70,p<0.01)
Model ensemble mean (r=0.38,p=0.05)
Model ensemble mean (r=0.72,p<0.01)
Model ensemble mean (r=0.65,p<0.01)
Europe
Oceania
South America
North America
El Chichón
Pinatubo
LAI Anomalies
Year
Trend in LAI
OBS
CO2
CLI
NDE
LCC
MMEM

Figure S11. The spatial distribution pattern of trend in growing season integrated LAI. (a) LAI derived from Multi-Model Ensemble Mean (MMEM) S1; (b) LAI derived from the difference of MMEM S2 and S1; (c) LAI derived from the difference of MMEM S3 and simulation S2. (d) LAI derived from the difference of MMEM S4 and S2. Regions labeled by black dots indicating those trends are statistically significant ($p<0.05$).

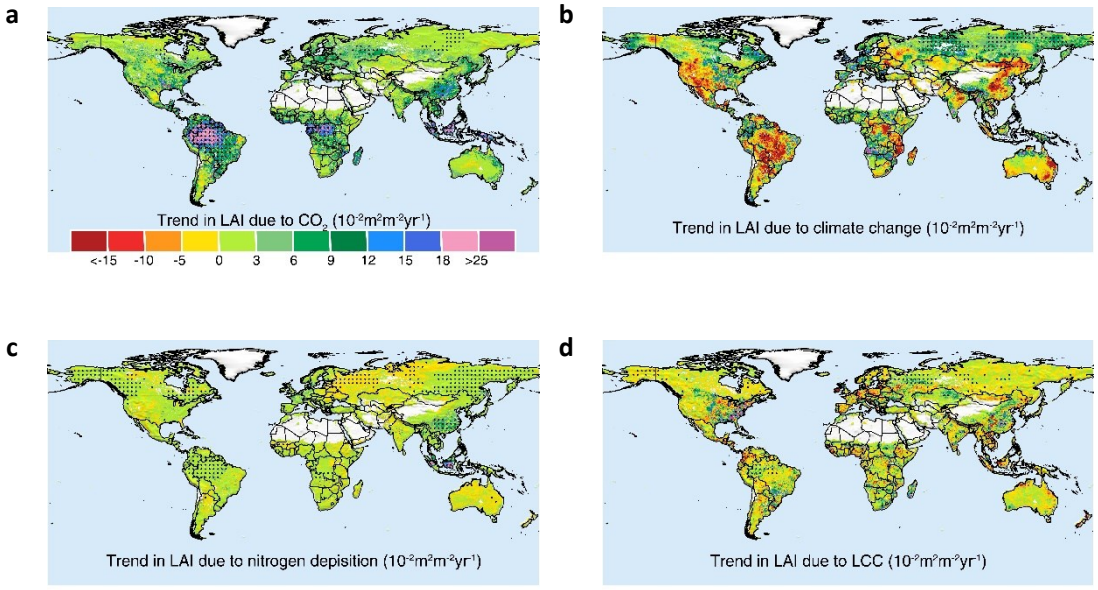

Figure S12. Spatial pattern of relative change of LAI due to CO_2 fertilization during 1982 to 2009. The relative change of LAI in each pixel is derived from the ratio of the increment of LAI driven by elevated atmospheric CO_2 to the 28-year average value of LAI simulated by model ensemble mean under scenario S1.

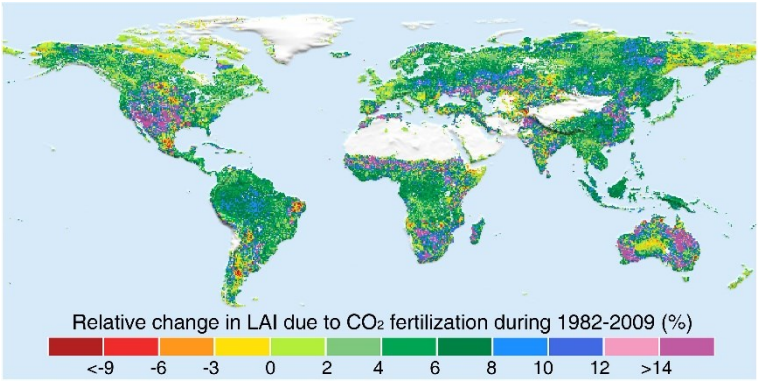

Figure S13. The spatial distribution pattern of primary driving climate factors of trend in growing season integrated LAI for the period 1982 to 2009. The dominant driving climate factor is defined as the climate factor that contribute the most to the increase (or decrease) in LAI in each vegetated grid-cell that dominated by climate change (-CLI and +CLI) defined in Fig. 3c. The driving climate factors include temperature (T), precipitation (P), and radiation (R). Prefixed '+' of driving factors indicate their positive effect on LAI trends, while '-' indicate negative effect. Vegetated pixels that dominated by factors other than climate change in Fig. 3c are shown in gray. Land pixels that have no vegetation are shown in white.